




## Article

# Catalytic Cracking of n-Hexadecane Using Carbon Nanostructures/Nano-Zeolite-Y Composite Catalyst

Botagoz Zhuman <sup>1</sup>, Shaheen Fatima Anis <sup>2</sup>, Saepurahman <sup>3</sup>, Gnanapragasam Singaravel <sup>4</sup> and Raed Hashaikheh <sup>2,\*</sup>

<sup>1</sup> Department of Chemical Engineering, Khalifa University of Science and Technology, P.O. Box 127788 Abu Dhabi, UAE; botagoz.zhuman@ku.ac.ae

<sup>2</sup> New York University Abu Dhabi (NYUAD) Water Research Center, NYUAD, P.O. Box 129188 Abu Dhabi, UAE; sfa5@nyu.edu

<sup>3</sup> Department of Chemistry, Institut Teknologi Bandung, Jl. Ganesha no. 10, Bandung 40132, Indonesia; saepurahman@chem.itb.ac.id

<sup>4</sup> ADNOC Refinery Research Centre (ARRC), P.O. Box 123593 Abu Dhabi, UAE; gnana@adnoc.ae

\* Correspondence: raed.hashaikheh@nyu.edu; Tel.: +971-2-6284626

Received: 25 September 2020; Accepted: 20 October 2020; Published: 28 November 2020



**Abstract:** Zeolite-based catalysts are usually utilized in the form of a composite with binders, such as alumina, silica, clay, and others. However, these binders are usually known to block the accessibility of the active sites in zeolites, leading to a decreased effective surface area and agglomeration of zeolite particles. The aim of this work is to utilize carbon nanostructures (CNS) as a binding material for nano-zeolite-Y particles. The unique properties of CNS, such as its high surface area, thermal stability, and flexibility of its fibrous structure, makes it a promising material to hold and bind the nano-zeolite particles, yet with a contemporaneous accessibility of the reactants to the porous zeolite structure. In the current study, a nano-zeolite-Y/CNS composite catalyst was fabricated through a ball milling approach. The catalyst possesses a high surface area of 834 m<sup>2</sup>/g, which is significantly higher than the conventional commercial cracking catalysts. Using CNS as a binding material provided homogeneous distribution of the zeolite nanoparticles with high accessibility to the active sites and good mechanical stability. In addition, CNS was found to be an effective binding material for nano-zeolite particles, solving their major drawback of agglomeration. The nano-zeolite-Y/CNS composite showed 80% conversion for hexadecane catalytic cracking into valuable olefins and hydrogen gas, which was 14% higher compared to that of pure nano-zeolite-Y particles.

**Keywords:** nano-zeolite; carbon nanostructures; composite catalyst; cracking

## 1. Introduction

Zeolite HY is a commercially important catalyst used widely in petroleum refining and petrochemical industries. H-Y zeolite has superior properties such as a 3D porous network containing channels and cages, high surface area, strong acidic sites, and high thermal and good hydrothermal stability [1]. These properties make zeolites a suitable catalyst for acid-catalyzed reactions, such as cracking and hydrocracking reactions of hydrocarbons [2,3]. In these processes, the zeolite is usually used in powder and extrudates forms [4], often containing and shaped in the presence of binders, such as alumina [5], clay [6], silica [7], titania [8], and phosphorus [9] or combinations of alumina and silica [10]. Those binders are generally present at higher than 20 wt.% to obtain an appropriate mechanical strength or to be shaped [11]. Alumina is mainly used as a zeolite binder in the preparation of catalyst extrudates, pellets, granules, flakes, and powder [12]. There are many limitations caused by conventionally used binders in the industry, the diffusion limitation being one of the important ones.

Poor diffusion can be caused by inhomogeneous distribution of the zeolite particles within the binding material, low surface area of the binders, and poor pore distribution within its structure [13]. Moreover, some binders can alter zeolite properties, in terms of acidity, which can affect overall selectivity and conversion [14]. Owing to the binder phases, catalysts in the extrudate form possess lower surface areas than bare zeolite particles. Usually, the surface area of alumina-supported industrial catalysts ranges from 60 to 100 m<sup>2</sup>/g [15]. Thus, most of the active area is lost in the binders. Catalytic reactions usually take place at high temperatures and pressures, thus the mechanical and thermal stabilities of the catalyst are important parameters. Mechanical properties are highly dependent on the type of binders used during the catalyst fabrication. However, commonly used binders for catalysts are brittle in nature, which makes them prone to fast attrition. Besides coking, attrition is found to be one of the reasons for fast catalyst deactivation [16].

Due to high surface area, less coking, and better mass transfer of the reactant and product molecules within the catalyst, nano-zeolite-Y has been reported to have a higher catalytic efficiency compared to zeolite-Y micro-particles [17,18]. Despite nano-zeolite having all these advantages, it tends to agglomerate during the catalytic process due to its high surface energy [19]. To overcome this limitation of nano-zeolites, they must be shaped into a different form, such as fibers [17]. Another approach of solving the agglomeration issue of nano-zeolites is using them in combination with various functional materials in the form of nanocomposites.

Progress in nanomaterials has paved the way for various carbon nanomaterials including carbon nanotubes (CNTs) [20], carbon nanofibers (CNFs) [21], fullerenes [22], and novel structured carbons [23]. Due to their superior chemical and physical properties, resistance to both acid and alkaline media, controllable porosity, and surface chemistry, carbon-based nanomaterials have successfully been reported as catalyst supports for various heterogeneous catalyst reactions [24–26]. Moreover, carbon-based binders have different anchoring sites for the attachment of active components, which gives better dispersion of the particles compared to conventionally used alumina binders [27]. Despite the fact that CNTs-supported catalysts are widely studied in the literature [27–30], a new approach of synthesizing a low-cost, flexible, and porous structure named carbon nanostructure (CNS) has paved the way for CNS nanocomposites. CNS has been proposed and developed by Applied Nano Structured Solutions LLC, a subsidiary of Lockheed Martin [31]. CNS refers to interdigitated, branched, and crosslinked CNTs that share common walls with one another. They possess good chemical, mechanical, electrical, and thermal properties, together with flexibility of the fibrous material.

CNS has been used as a binding material with lithium iron phosphate (LiFePO<sub>4</sub>) particles as battery electrodes [32,33]. A cathode with high loadings of the active material was achieved. Moreover, homogeneous distribution of LiFePO<sub>4</sub> particles within the CNS network facilitated a fast charge transfer and increased the conductivity and diffusion coefficient of the cathode [32]. Therefore, it is expected that using CNS as a binding material provide homogeneous distribution of the particles due to its fibrous structure and can prevent blocking of its active sites. This can address the agglomeration issue of zeolite particles commonly caused by conventionally used binders, such as alumina. Another advantage of using CNS as a binder is to prevent a reduction in the surface area of the composite catalyst, as CNS has a higher surface area [32], compared to alumina binders. In addition, the flexibility of the fibrous structure and superior properties of CNS allow catalysts to be shaped in different forms, which increases its mechanical stability and prevents attrition and chipping of the catalyst during the catalytic process.

In this work, CNS is used as a binding material for zeolite nanoparticles. These zeolite nanoparticles were produced through a ball milling approach, reported previously by our group [34]. The ball-milled nano-zeolite with a high Si/Al ratio of 15 has also been previously reported for hydrocracking [3,17], as an electrocatalyst [18], and in water treatment [35,36] applications. This work studies the catalytic activity of a CNS/nano-zeolite-Y composite catalyst and compares it with the catalytic activity of nano-zeolite-Y particles alone for n-hexadecane cracking reaction. Cracking of alkanes by zeolite plays a central role in the production of fuels from petroleum. Several parameters such as catalyst activity,

selectivity of the products, stability of the catalyst, coking, and catalyst deactivation tendencies have been studied and reported. The following abbreviations are used hereafter in the paper: nano-zeolite-Y particles—"NHYZ", and nano-zeolite-Y/CNS composite—"NHYZ/CNS".

## 2. Results

### 2.1. Surface Morphology and Elemental Mapping

Figure 1a–c shows SEM images of NHYZ, CNS, and NHYZ/CNS. The SEM image of the composite showed that zeolite nanoparticles are highly entangled within CNS bundles. Zeolite nanoparticles were seen to be present in different sizes (Figure 1a), as previously reported in [34]. From the SEM image of the NHYZ/CNS composite (Figure 1c), it can be seen that using CNS as a binding material can form a highly homogeneous structure which can bind nano-zeolite particles together, meanwhile creating a porous and open network for efficient diffusion of the feed molecules to the active sites of zeolite. Further, SEM-EDS analysis of an industrial catalyst extrudate was performed in order to study the uniformity in distribution of the catalyst and the binder. Figure S1 reveals the inhomogeneous distribution of zeolite particles within alumina. In addition, non-uniform distribution of tungsten (sulphide form) was also observed. This is one of the major causes for the inaccessibility of active sites, which is usually hindered because of the binding material. Meanwhile, the NHYZ/CNS composite showed great dispersion of nano-zeolite-Y particles in the CNS matrix (Figure 2). The detected elements Al, Si, and O are due to the zeolite, while C was detected from CNS.

### 2.2. Surface Area

Figure 3 shows the N<sub>2</sub> adsorption–desorption curves for NHYZ particles, CNS, and NHYZ/CNS. BET surface areas for NHYZ and CNS were 1190 and 223 m<sup>2</sup>/g, respectively. The surface area of the composite catalyst is highly dependent on the surface area of its components and was found to be 834 m<sup>2</sup>/g. It can be seen from the graphs that catalysts have a mesoporous structure, typical of most zeolites [37].

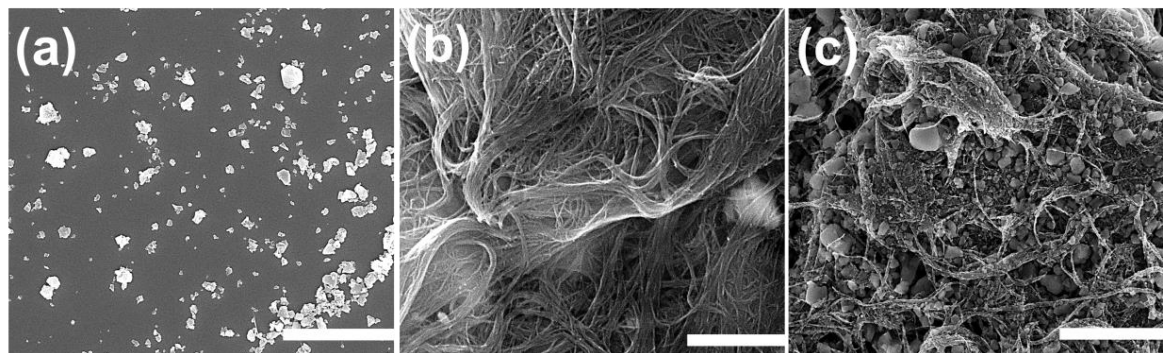


**Figure 1.** SEM images of (a) nano-zeolite-Y particles (NHYZ), scale bar = 3  $\mu\text{m}$ , (b) carbon nanostructure (CNS), scale bar = 1  $\mu\text{m}$ , and (c) NHYZ/CNS, scale bar = 3  $\mu\text{m}$ .



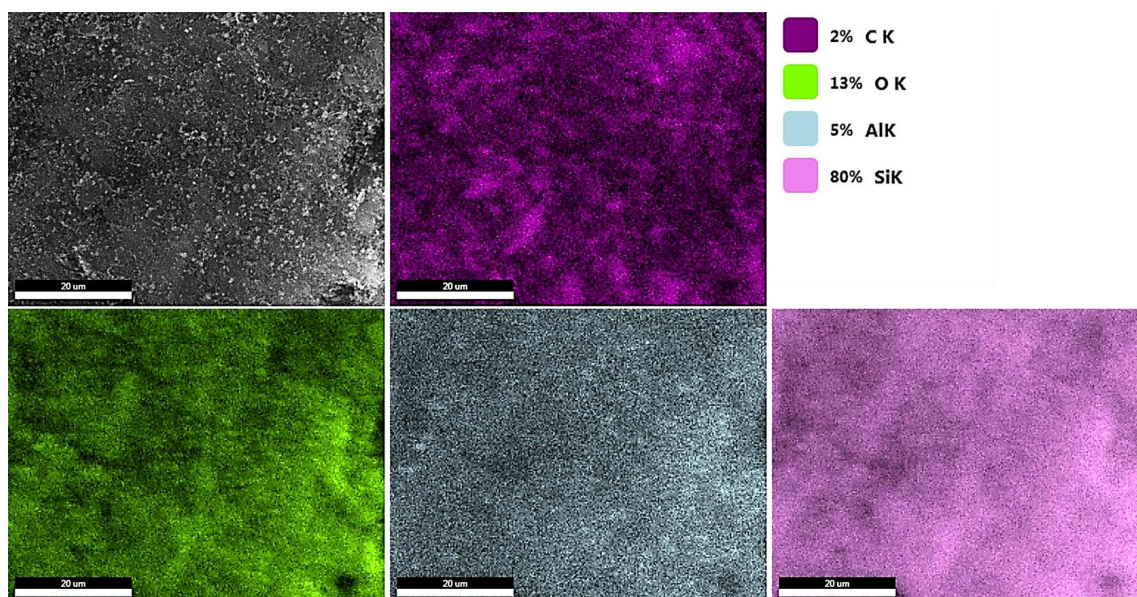


Figure 2. EDS analysis of the NHYZ/CNS catalyst, scale bar = 20  $\mu\text{m}$ .

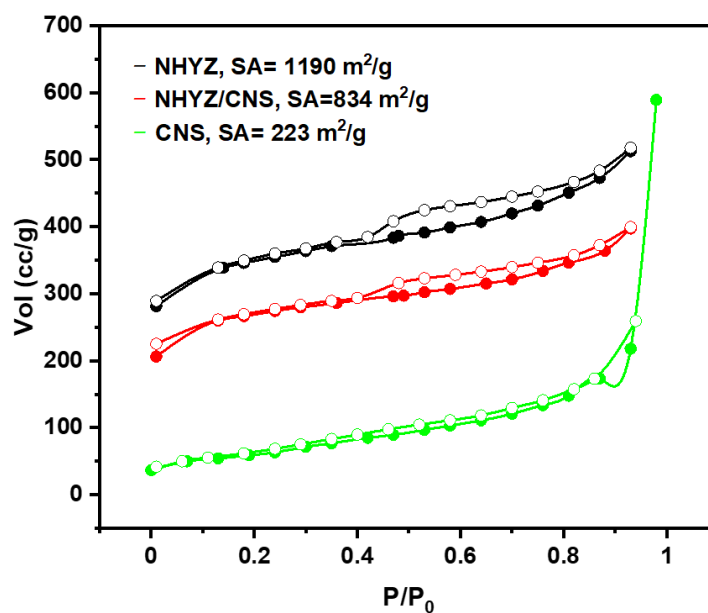


Figure 3.  $\text{N}_2$  adsorption/desorption isotherm of NHYZ, NHYZ/CNS, and CNS, filled circles represent adsorption and empty circles represents desorption, SA = surface area.

### 2.3. X-ray Diffraction Analysis

Figure 4 represents the XRD graph for NHYZ, NHYZ/CNS, and CNS materials. CNS shows two characteristic amorphous peaks at 25.7 and 42.7 degrees, whereas NHYZ has crystalline characteristic peaks of HY zeolite at 15.7, 18.7, 23.7, 27.1, 30.8, 31.5, and 34.2 degrees. NHYZ/CNS retained all of the characteristic peaks of NHYZ and has amorphous peak broadening around 25.5 degrees.

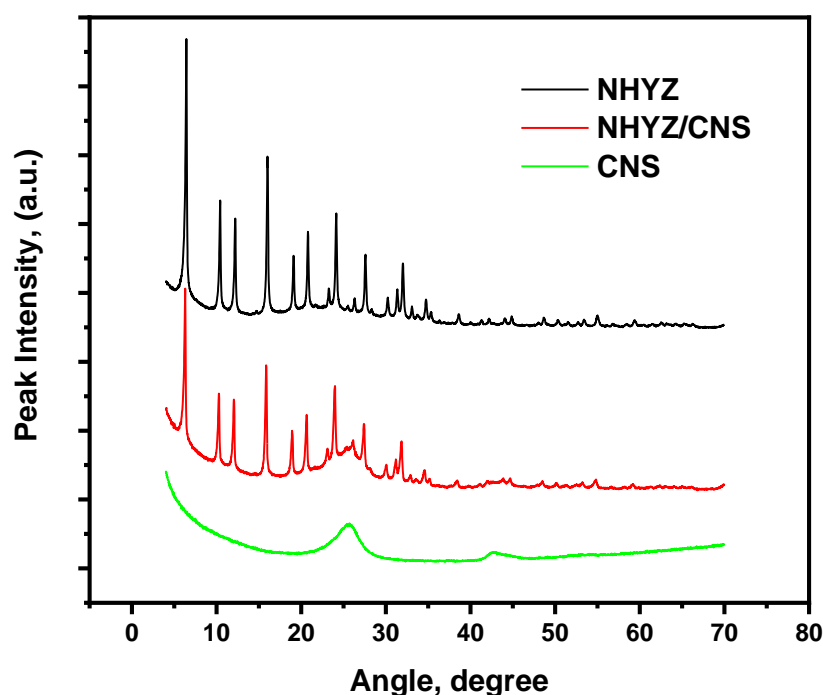


Figure 4. XRD graph of NHYZ, CNS, and NHYZ/CNS.

#### 2.4. Catalytic Performance and Coke Formation

Percentage of total conversion for n-hexadecane is shown in Table 1, while Figure 5 shows the total conversion over time for both catalysts. The NHYZ/CNS composite has a higher conversion rate (80%) during the 1-h time on stream (TOS) compared to the NHYZ catalyst (66%). The activity of NHYZ/CNS is maintained over 3 h, as the conversion rate decreases by only 4%. Moreover, NHYZ/CNS has a lower deactivation compared to NHYZ which was 10% over 3 h. Deactivation is mainly caused by blockage of the active sites by coke. Similar catalyst deactivation has been reported in [17]. Considering that cracking reactions are happening at high temperatures, it is important to highlight that thermal cracking could also be involved. However, in our study, thermal cracking gave several by-products, such as n-hexane, pentadecane, and hexadecene, with only 4% hexadecane conversion at 514 °C.

Table 2 show the product range for the n-hexadecane cracking reaction over 3 h including gaseous and liquid products (GP and LP) and coke. Figure 6 presents the amount of each product formed after each hour of catalytic cracking by NHYZ and NHYZ/CNS catalysts. NHYZ/CNS had two times higher formation of LP (11.5 wt.%) and 9 wt.% higher cracked GP compared to NHYZ during the first hour of TOS. Selectivity of products is different for both of the catalysts, as can be seen in Table 3 and Figures 7 and 8. NHYZ/CNS showed a high production of hydrogen gas around 40 wt.% over 3 h of TOS (Figure 8), whereas NHYZ had paraffin as its major products, equal to 36.6 wt.% during the first hour of TOS (Figure 7). This is due to the different mechanisms of cracking of n-hexadecane for NHYZ/CNS and NHYZ catalysts. The NHYZ/CNS composite is found to be the superior catalyst for hydrogen production and had an active dehydrogenation process compared to NHYZ.

Table 1. Conversion rates for NHYZ and NHYZ/CNS catalysts.

Catalyst Name	NHYZ	NHYZ/CNS
Hours	Conversion %	
1	66	80
2	62	77
3	56	76

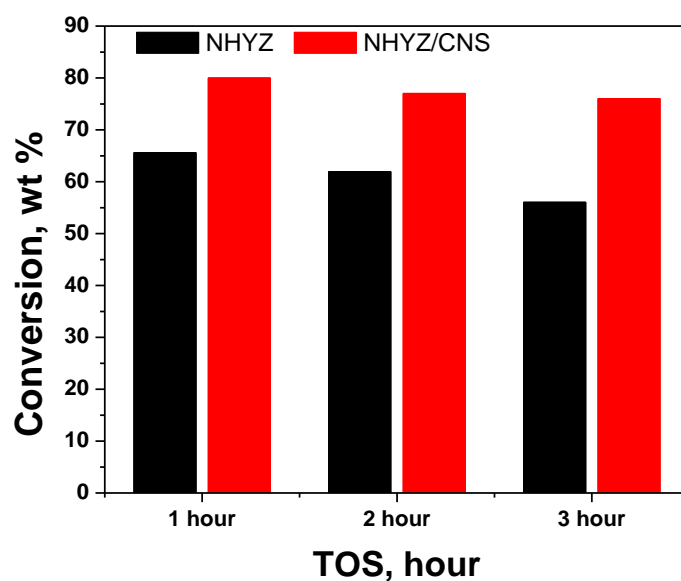


Figure 5. Conversion rates for NHYZ and NHYZ/CNS catalysts.

Table 2. Gaseous and liquid products (GP and LP) for NHYZ and NHYZ/CNS catalysts.

TOS	Gaseous Products (GP), wt. %	Liquid Products (LP), wt. %	Coke after 3 h TOS, wt. %
NHYZ			
1	59.3	6.3	0.8
2	55.6	6.4	
3	46.2	9.8	
NHYZ/CNS			
1	68.2	11.5	3.4
2	63.6	13.1	
3	62.6	13.1	

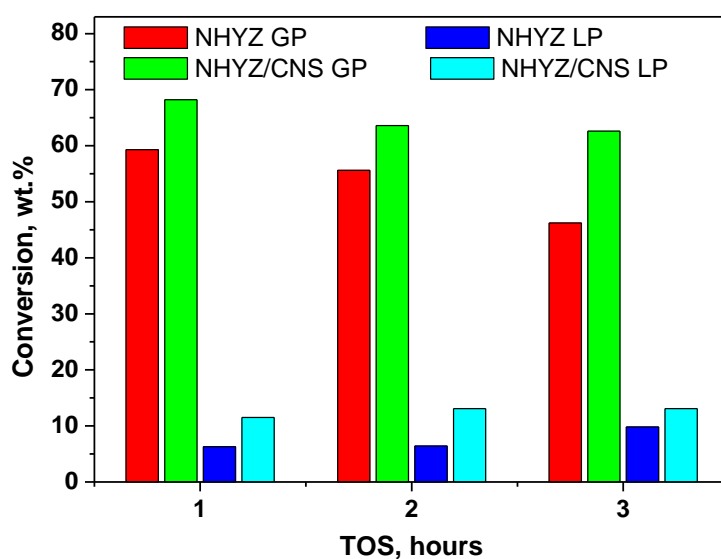


Figure 6. GP and LP for NHYZ and NHYZ/CNS catalysts.

**Table 3.** Selectivity of NHYZ and NHYZ/CNS catalysts.

Catalyst	NHYZ			NHYZ/CNS		
TOS	1	2	3	1	2	3
Paraffins	36.6	33.3	30.5	17.5	12.7	12.9
Olefins	21.3	21.9	19.1	14.1	10.3	8.9
Aromatics	4.2	3.2	3.3	7.9	6.2	7.1
Hydrogen	3.3	3.2	2.7	39.4	46.6	45.9

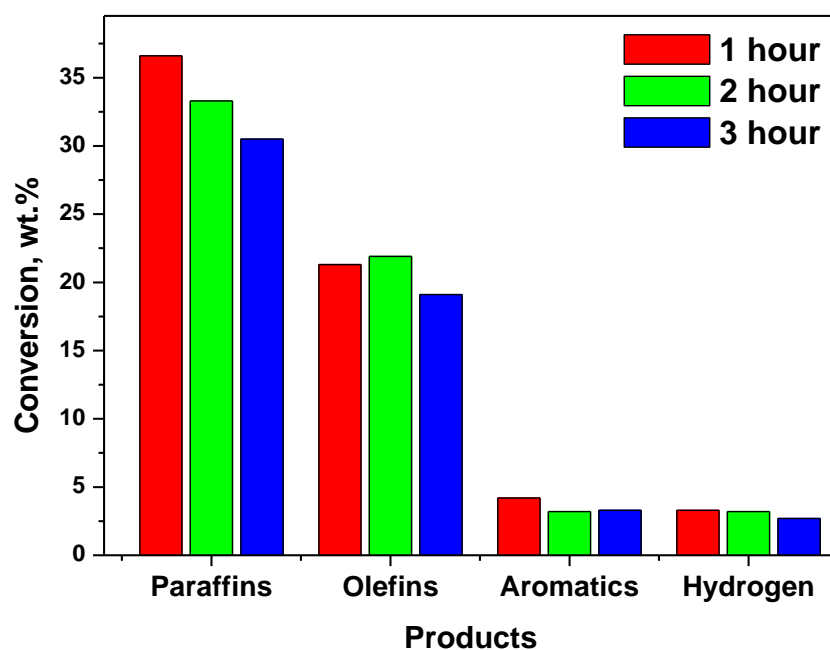
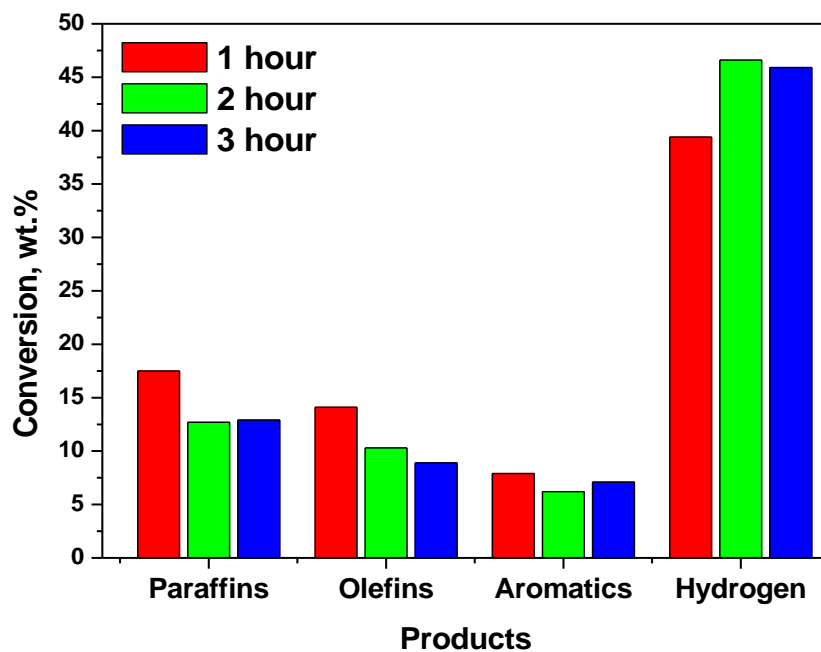
**Figure 7.** Selectivity of the NHYZ catalyst.**Figure 8.** Selectivity of the NHYZ/CNS catalyst.

Figure 9 shows the carbon number of products cracked at the end of each hour for both the catalysts. The carbon number of the products agrees well with the literature [38,39]. The majority of

the products are in the diapason of  $C_1$  and  $C_7$ , while the products with a carbon number higher than 7 were less than 1%. Isobutane was the major cracked product for NHYZ during the first hour of TOS (12.49 wt.%), whereas propylene was the major hydrocarbon (HC) product for NHYZ/CNS (9.66 wt.% during the first hour of TOS) and was found to be the dominant product after the initial hour for both the catalysts.  $C_3$  and  $C_5$  paraffins were found to be the second major products after propylene for both catalysts. Carbon numbers for paraffins and olefins are shown in Tables S1 and S2, respectively.

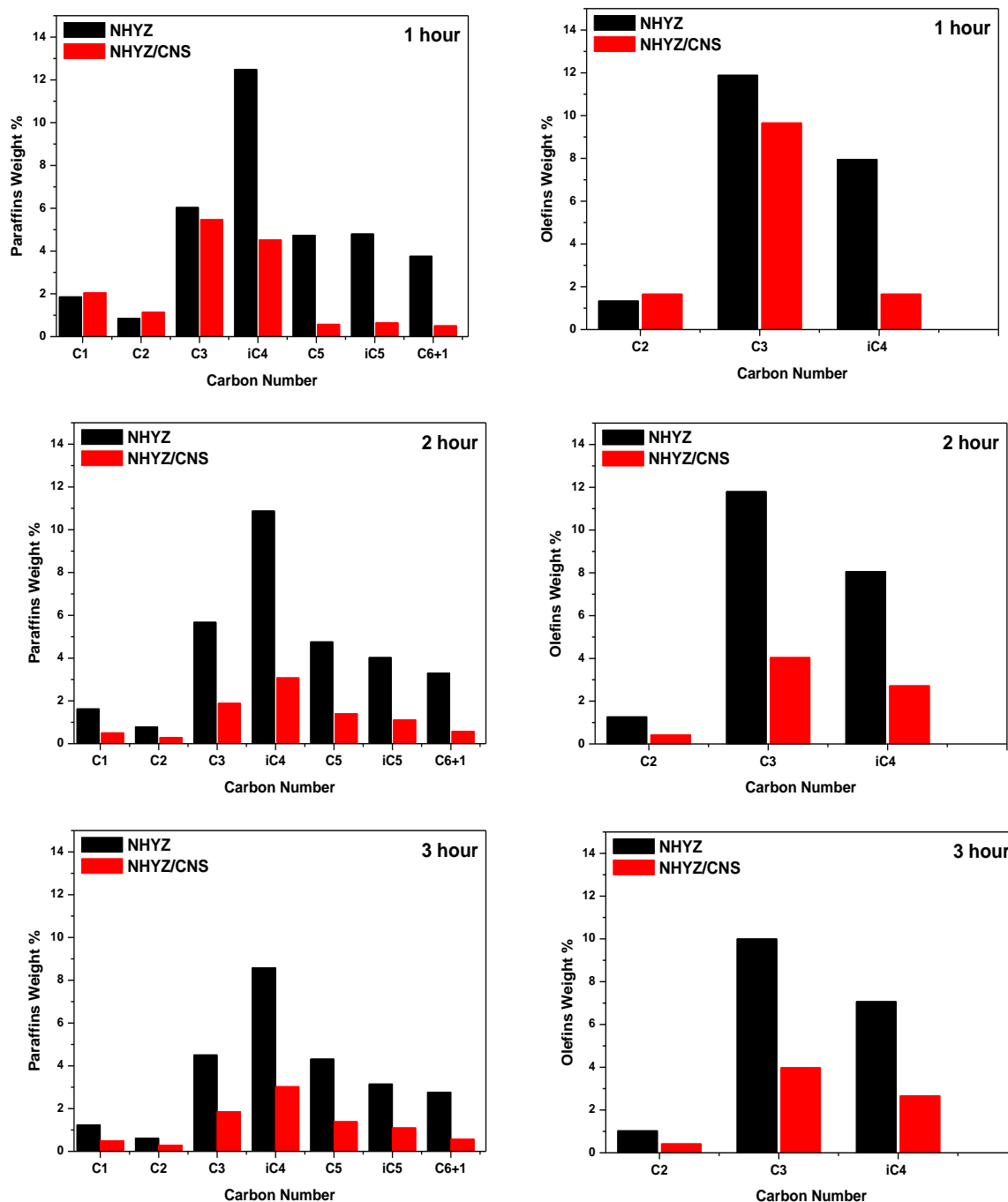


Figure 9. Paraffins and olefins carbon number in GP of NHYZ and NHYZ/CNS catalysts.

Coke formation has been studied using TGA (Figure 10) of fresh and spent catalysts. Here, 3.4 and 0.8 wt.% of coke were calculated for NHYZ/CNS and NHYZ catalysts, respectively. The TGA graph of CNS alone is shown in Figure S2 and the decomposition temperature is equal to 581 °C (Table



S3). Higher formation of coke for NHYZ/CNS can be explained by the overall higher conversion of the feed compared to NHYZ and the more significant hydrogen transfer process. Coked catalysts were analyzed using SEM as shown in Figure 11. Figure 11a shows that the spent NHYZ catalyst formed agglomerates after the cracking reaction. From Figure 11b, it can be observed that nano-zeolite particles remained attached to CNS bundles.

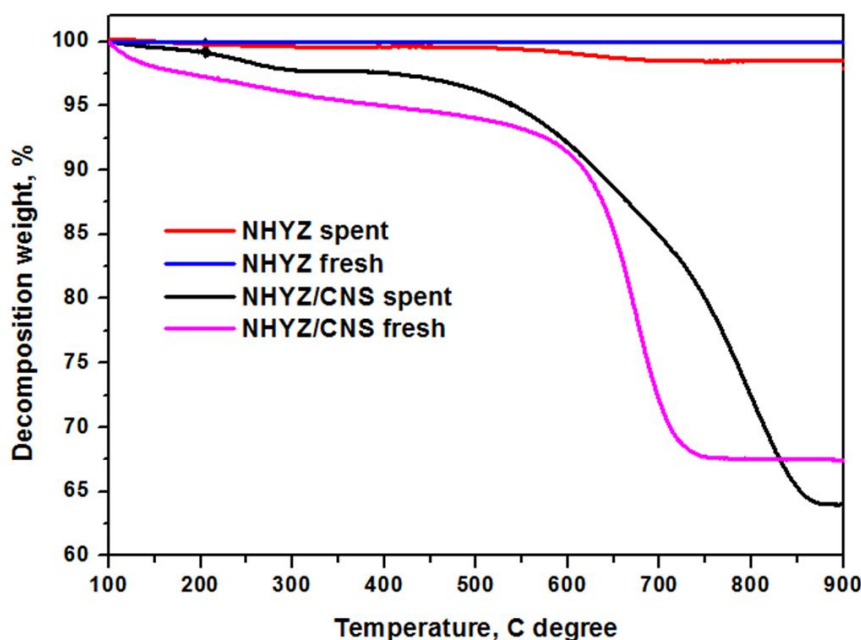


Figure 10. TGA analysis of fresh and spent NHYZ and NHYZ/CNS catalysts.

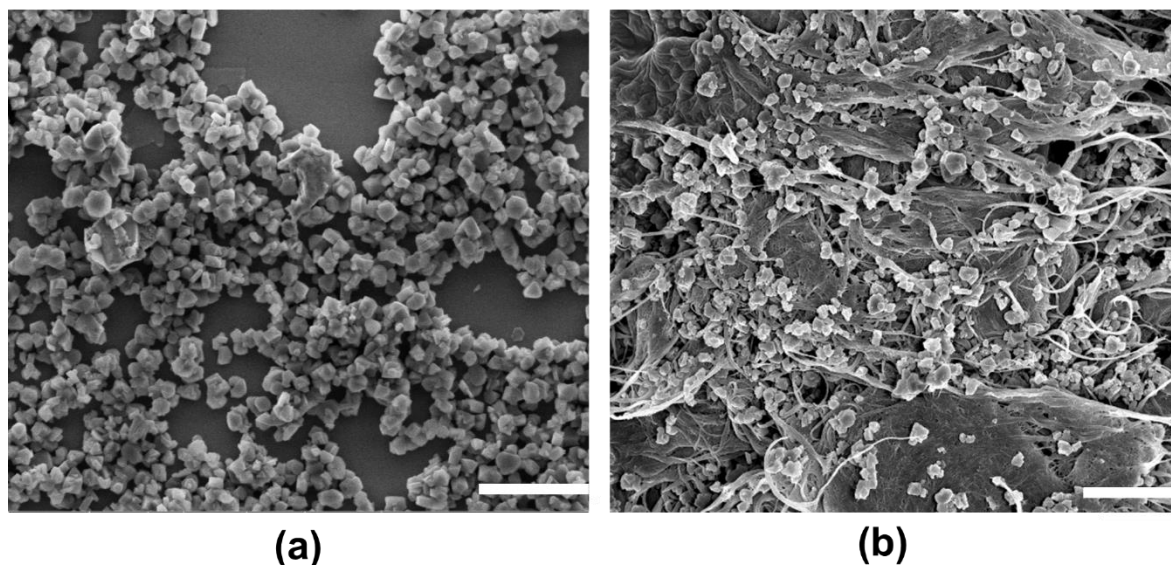


Figure 11. SEM images of coked catalysts: (a) NHYZ, and (b) NHYZ/CNS, scale bar = 5 µm.

### 3. Discussion

Using CNS as a binding material can form a highly homogeneous structure (Figure 1c), and can overcome the limitations caused by agglomeration of active components. CNS binds nano-zeolite particles together, meanwhile creating a porous and open structure for efficient diffusion of the feed molecules to the active sites of zeolite. This, in essence, overcomes the limitations caused by commonly used binders [40]. The macroporous structure of CNS can benefit the mass transport process of the

feed to active sites of nano-zeolite-Y. In addition, the composite catalyst has a high surface area of 834 m<sup>2</sup>/g, and it is higher compared to common alumina-supported industrial catalysts [4] which can range from 60 to 100 m<sup>2</sup>/g [15]. Table 4 represents surface areas of nano- and micro-zeolite-Y used as fluid catalytic cracking (FCC) catalysts shaped with Al<sub>2</sub>O<sub>3</sub>, SiO<sub>2</sub>, or SiO<sub>2</sub>/Al<sub>2</sub>O<sub>3</sub> as binders. The surface area of an industrial catalyst is highly dependent on the surface area of its binders and ranges from 200 to 350 m<sup>2</sup>/g, while the surface area of Al<sub>2</sub>O<sub>3</sub> itself ranges between 200 and 270 m<sup>2</sup>/g [41,42]. However, using SiO<sub>2</sub>/Al<sub>2</sub>O<sub>3</sub> binders for nano-zeolite-Y results in a loss of active surface area and coverage of the nano-particles with the binding material. The developed NHYZ/CNS composite has three times higher surface area compared to the reported industrial FCC cracking catalysts. This shows that using CNS as a binding material can form a highly efficient composite with a high surface area.

**Table 4.** Surface areas of nano- and micro-zeolite-Y-based fluid catalytic cracking (FCC) catalysts.

No	FCC Catalyst	Surface Area, m <sup>2</sup> /g	Reference
1	Nano-Y zeolite in SiO <sub>2</sub> /Al <sub>2</sub> O <sub>3</sub> matrix	230	[43]
2	Nano-zeolite-Y in SiO <sub>2</sub> binder	315 (nano-zeolite-Y original surface area 570)	[44]
3	Micro-zeolite-Y-supported Al <sub>2</sub> O <sub>3</sub>	341 (zeolite-Y original surface area 672)	[45]

Moreover, using CNS as a binding material does not alter and can preserve the crystalline structure of NHYZ (Figure 4). XRD analysis shows all nano-zeolite-Y characteristic peaks for the NHYZ/CNS composite. Unlike while using Al<sub>2</sub>O<sub>3</sub> as a binder, all the crystalline characteristic peaks of nano-zeolite-Y have disappeared, showing only Al<sub>2</sub>O<sub>3</sub> peaks for the composite catalyst after shaping with a binder [46]. On the other hand, using CNS as a binder creates a highly accessible porous structure for nano-zeolite-Y while retaining the crystallinity of the catalyst.

Additionally, the homogeneous dispersion of nano-zeolite particles, maintained crystalline structure, and high surface area of the catalyst can serve for increased efficiency of the overall catalyst. A high conversion of 80% for NHYZ/CNS can be another evidence of the highly dispersed and homogeneous structure of the composite created after the ball milling process [34,47] which provided a higher accessibility to active sites for the reaction with feed molecules. This could also be explained due to the faster diffusion for nano-sized zeolite particles created after the ball milling process [34,47]. Meanwhile, NHYZ had lower conversion (66%) compared to NHYZ/CNS, possibly due to having nano-zeolite particles agglomerated during the catalytic process. Besides, NHYZ had a higher deactivation rate of 10% during the 3 h of TOS, which is 6% higher than NHYZ/CNS. Despite NHYZ having a much higher surface area than NHYZ/CNS, the conversion rates showed an inverse trend. This might be due to the fact that NHYZ agglomerates during the catalytic cracking reaction, which will not allow the feed to reach all of the active surface area of NHYZ. Moreover, this also shows that nano-zeolite has higher catalytic efficiency in the form of the NHYZ/CNS composite which prevents nanoparticles from agglomeration and creates a more efficient catalyst with higher accessibility of active sites of nano-zeolite to the feed.

Both catalysts gave a different selectivity of products (Figures 7 and 8). Figure 8 shows that NHYZ/CNS serves as an efficient catalytic cracking catalyst for the production of highly valuable alkenes and hydrogen gas. Product distribution of NHYZ/CNS and NHYZ catalysts can be interpreted by protolytic cracking [48],  $\beta$  scission, dehydrogenation, and hydrogen transfer [38]. Primarily n-hexadecane is adsorbed into the pore of zeolite, then it undergoes cracking at Bronsted (H<sup>+</sup>) and Lewis acid (tricoordinated aluminium or/and AlO<sup>+</sup>) sites [49]. Protolytic cracking is kinetically dominant in the initial steps and it is originated at the Bronsted acid (H<sup>+</sup>) site of zeolite to form penta-coordinated carbonium ion. Further C-C bond breaking results in paraffin in gaseous form and adsorbed carbenium ion. Major products for both the catalysts are in the gaseous form for the total TOS, as shown in Table 2 and Figure 6. Both catalysts form an overall higher concentration of paraffins compared to olefins during the 3 h of the cracking reaction, as can be seen in Table 3 and Figures 7 and 8. Further rearrangement of carbenium ion leads to the formation of branched paraffins.

Formation of branched species of olefins is attributed to the participation of Lewis acid sites during the initiation of cracking, forming as a result a carbenium ion which desorbs as a branched olefin, if this carbenium ion has four or more carbon atoms. Formation of iso-butene is higher for NHYZ during the first hour compared to NHYZ/CNS, whereas the concentration of isobutene increases for NHYZ/CNS after the first hour of TOS (Figure 9 and Table S2).

Hydride transfer between the feed molecule (n-hexadecane) and adsorbed carbenium ion leads to further cracking via  $\beta$  scission, causing a chain reaction [50,51]. The chain reaction gives a higher concentration of olefins. Table 3 shows an increase in the concentration of olefins for 2-h TOS for NHYZ. However, it is not the case for NHYZ/CNS due to the significant dehydrogenation or formation of hydrogen gas. Figure 8 shows the concentration of formed hydrogen gas for the NHYZ/CNS catalyst. Production of hydrogen gas was observed as one of the major products for NHYZ/CNS compared to NHYZ. During the 1-h TOS, 39.4 wt.% of  $H_2$  was obtained as a product. It increased until 48–47 wt.% during 2- and 3-h of TOS, whereas NHYZ  $H_2$  accounted for 3.3–2.7 wt.% during the 3-h TOS. Formation of hydrogen gas can be a result of the C-H bond cleavage by the Bronsted acid ( $H^+$ ) site of zeolite which results in formation of  $H_2$  and carbenium ion [50]. The other possible source of hydrogen gas is the (-OH) groups of the catalyst. The selectivity results (Table 3) suggest that protonation is happening at the C-H bond and is dominant for the NHYZ/CNS catalyst which gives a higher amount of  $H_2$ , whereas primary protonation for NHYZ is initiating on the C-C bond, resulting in a higher concentration of paraffins. Formation of molecular hydrogen ( $H_2$ ) during the cracking reaction of alkanes by superacid catalysts has been extensively reported by Oleh et al. [52–54].

Formation of aromatics and coke can be explained by a secondary reaction or hydrogen transfer. If the paraffin/olefin (P/O) ratio is higher than 1, it signifies a hydrogen transfer process. Considering the P/O ratio of NHYZ, hydrogen transfer is more significant for NHYZ compared to NHYZ/CNS. However, if the concentrations of coke and aromatics are considered, then NHYZ/CNS has the more dominant hydrogen transfer compared to NHYZ. On the other hand, NHYZ/CNS has higher total conversion of the feed, which will result in higher concentrations of coke and aromatics. The proposed reaction mechanism is depicted in Figure 12 and all products formed after n-hexadecane cracking are shown in Figure 13.

Generally, for both of the catalysts, hydrogen transfer is dominant during the first hour and leads to the formation of unsaturated species such as aromatics and coke, as shown in Tables 2 and 3 [55]. However, it is less dominant after the first hour since the concentration of aromatics decreases for both of the catalysts, as can be seen from Figures 7 and 8.

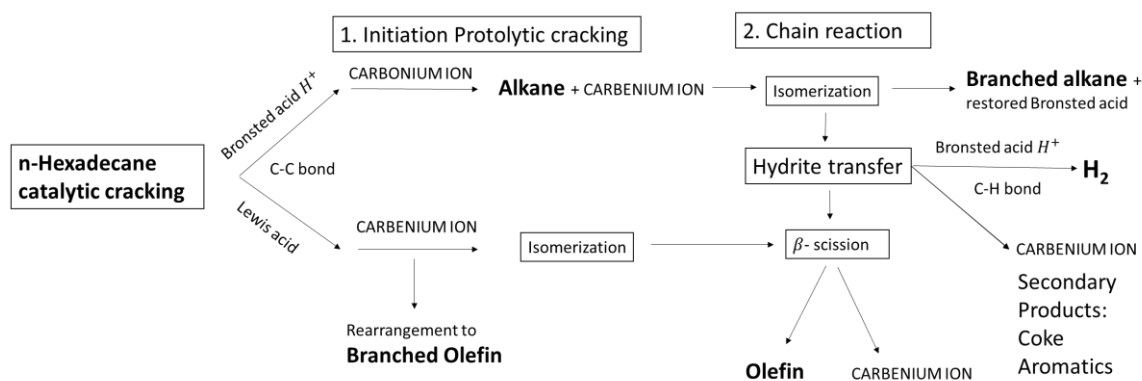


Figure 12. Proposed reaction mechanism of n-hexadecane cracking.

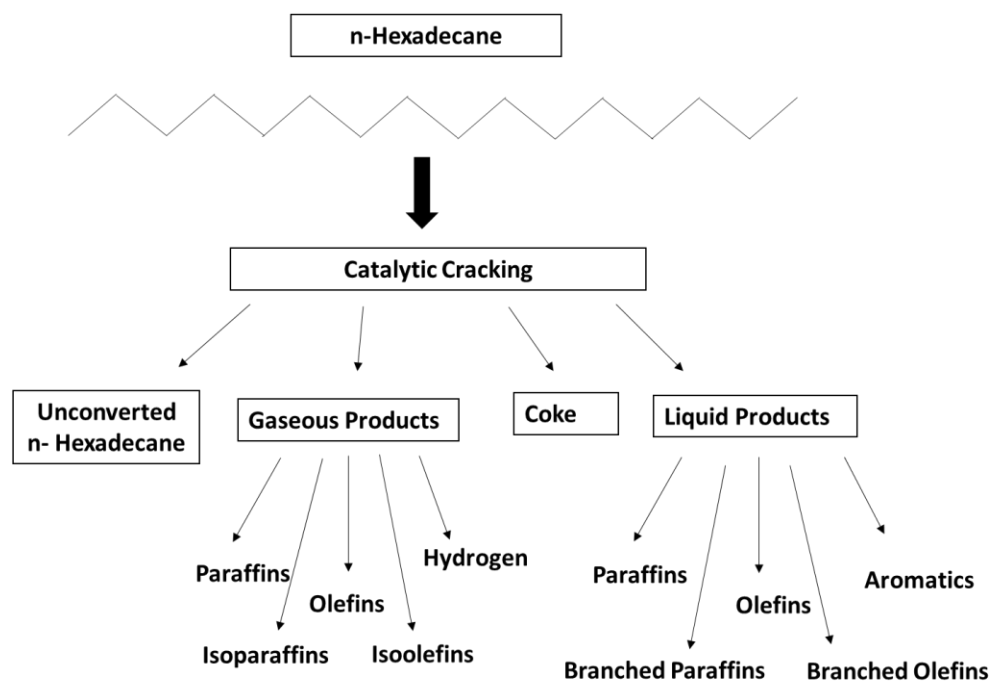


Figure 13. Products of n-hexadecane catalytic cracking.

Product distribution shows that propylene was the major HC product formed for the NHYZ/CNS composite catalyst during the 3-h TOS. It is important to note that the production of light olefins such as propylene, n-butene, and isobutene is highly desirable and is one of the global targets for fluid catalytic cracking (FCC) units. These types of olefins can be useful for further etherification and alkylation processes to produce more environmentally friendly gasoline products. The aromatic products produced were toluene, benzene, naphthalene, cymene, and xylenes, where benzene was the dominant product.

In order to endure the collisions happening inside the reactor in an industrial catalytic cracking unit, the catalyst should have enough hardness and yet need to be flexible to prevent attrition from happening. Apart from that, the composite catalyst should maintain its structure after the cracking reaction which can prove its mechanical stability under harsh conditions. Usually industrial FCC catalysts are shaped in the form of extrudates, spheres, granules, etc. However, catalysts in this form tend to attire and chip under harsh conditions inside the reactor. Commonly used industrial catalysts are brittle in nature and lack flexibility. Therefore, using a flexible, fibrous, and mechanically stable binding material allows the catalyst to be shaped into different forms, while reducing its tendency to chip and attire. Moreover, it can increase the mechanical stability of the composite catalyst -by effectively forming a highly bonded structure. SEM images of coked catalysts (Figure 11) illustrate that the composite catalyst is mechanically stable under harsh conditions. This proves the efficiency of CNS as a binding material for the shaping of catalysts and that it could be used as a successful physical functionalization method for the fabrication of zeolite/CNS composites. Additionally, it proves that CNS can provide the matrix which prevents nanoparticles from agglomeration. It can be seen that NHYZ/CNS forms a highly bonded composite. The physical-form NHYZ/CNS catalysts can be observed to be intact, with no major changes, after the catalytic cracking reaction in the micro-catalytic reactor, thus attesting to the physical stability of the NHYZ/CNS catalyst.

Another important factor that needs to be considered is that CNS would be removed through the calcination step during the regeneration process of the catalyst. Therefore, more studies are required in order to lower the concentration of CNS during the fabrication process while retaining the same efficiency and homogeneous distribution within the composite.



## 4. Materials and Methods

### 4.1. Materials

Ultra-stable Zeolite-Y (CBV-720) with a  $\text{SiO}_2/\text{Al}_2\text{O}_3$  ratio of 30 was procured from Zeolyst International and used as a parent zeolite. Nano-sized ball-milled zeolite-Y was obtained by ball milling (high-energy ball mill Emax, Retsch, Haan, Germany) the parent zeolite particles with CNS. The procedure reported in [34] was followed. Ethanol,  $\geq 99\%$ , was purchased from Sigma Aldrich. Deionized (DI) water was produced using the Suez/Purite Neptune Ultimate Water Purification Machine. n-Hexadecane,  $\geq 99\%$ , was purchased from Sigma Aldrich and used for catalytic testing. Carbon nanostructures (CNS) were supplied by Lockheed Martin with a bulk density of  $0.015 \text{ g/cm}^3$  and incorporated CNTs with a length of  $1\text{--}10 \text{ }\mu\text{m}$ .

### 4.2. Preparation of Composite Catalyst Using Ball Milling

NHYZ was obtained through a ball milling process, reported previously by our group [17,18,34–36].

The NHYZ/CNS composite was fabricated using the following procedure depicted in Figure 14. Ball milling was carried out in zirconia jars using 2 mm zirconia balls. Commercial zeolite-Y particles and CNS were used in the ratio of 75:25 by weight in a solvent ratio of water/ethanol of 1:1 by volume. Ball milling was performed at 1000 rpm for 1 h. Ball-milled samples were centrifuged (Thermo Scientific, Heraruss Megafuge 40R, Langenselbold, Germany) at 4000 rpm for 5 min, and the bottom part of the sample was selected for this study. The bottom part was selected due to having a higher yield, surface area, and crystallinity of the zeolite particles. Zeolite yield, surface area, and crystallinity of the material have been previously reported by our group [34]. Centrifugation was followed by drying under vacuum at  $80^\circ\text{C}$  overnight.

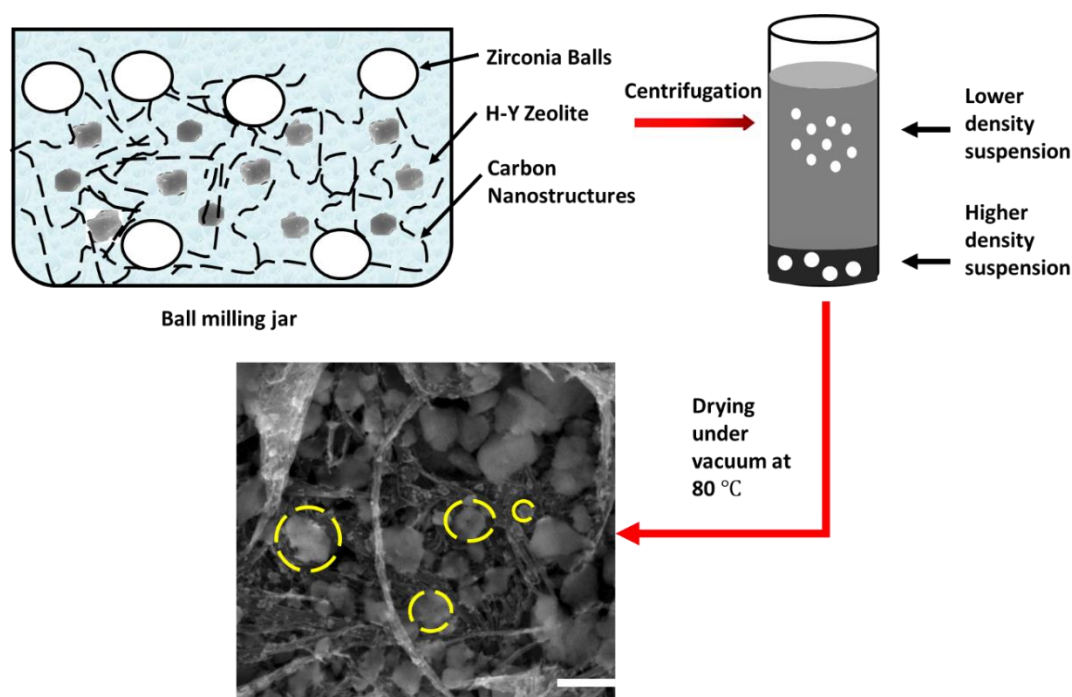


**Figure 14.** Composite catalyst fabrication procedure using ball milling. Ball-milled zeolite particles are indicated by yellow dashed circles, scale bar = 500 nm.

### 4.3. Characterization

Surface morphology and elemental analysis were analyzed using high-resolution scanning electron microscopy (HRSEM) (Nova Nano SEM, FEI, Eindhoven, The Netherlands) and an energy-dispersive

X-ray spectrum (EDS) (EDXS, FEI, Eindhoven, The Netherlands). Surface area was measured by multi-point Brunauer–Emmett–Teller (Quantachrome, NOVA 2000e, Boynton Beach, FL, USA) (BET) surface and pore size analyzer. Surface area (BET) was calculated using  $P/P_0$  regimes from 0.05 to 0.35. Thermo-gravimetric analysis (TGA) of the coked and fresh catalysts was performed using Perkin Elmer TGA 4000 (Waltham, MA, USA). A total of 10–20 mg of the sample was heated until 900 °C under oxygen flow of 20 mL/min at a 10 °C/min heating rate. XRD analysis was performed using XRD PANalytical Empyrean (Almelo, the Netherlands), and the scan was performed between 5 and 70° at a scan rate of 3 degrees per min.

#### 4.4. Catalytic Testing

n-Hexadecane catalytic cracking was carried out in a steady-state fixed-bed micro-catalytic reactor (custom made by Sigma Enterprises LLC, Abu Dhabi, United Arab Emirates). Thermocouples were placed in the top, middle, and bottom of the catalytic bed to measure the temperature distribution, whereas the flow rates of the gas and feed were controlled by mass flow controllers. The catalyst mass of 0.86 g was used for all experiments, with a weight hourly space velocity (WHSV) of 2.68 h<sup>−1</sup>. NHYZ particles and the NHYZ/CNS composite were tested in powder form. The catalyst activation process was carried out at 514 °C in a helium atmosphere. After 3 h of activation, liquid feed was inserted along with helium. The temperature was raised to 514 °C and kept constant thereafter. The rate of hexadecane feed was set at 0.05 cc/hr. The reaction was carried out for 3 h at an atmospheric pressure of 1 bar. Liquid and gaseous products were collected separately. The weight of LP was recorded at every 1 h interval and was analyzed offline using a gas chromatograph mass spectrometer (GC 7890B-MS5977A) equipped with a 5-column nonpolar column. The GP were also collected at every hour interval and analyzed by an offline GC system (7890A GC system, 8-column RGA with a FID detector). Percentage conversion and selectivity were calculated using the following equations:

$$\% \text{ Conversion} = \frac{\text{Initial feed (g)} - \text{Final feed (g)}}{\text{Initial feed (g)}} \times 100 \quad (1)$$

$$\% \text{ Selectivity} = \frac{\text{Mass of individual product (g)}}{\text{Initial feed (g)} - \text{final feed (g)}} \times 100 \quad (2)$$

Carbon number in the products was calculated based on the weight of the individual products. The mass balance was calculated in accordance with GP and LP and coke that formed, and the remaining accounted for loss of HC products during the testing and collection of the samples which is evident from the results.

## 5. Conclusions

In this study, CNS was used as a binding material for nano-zeolite-Y. Using CNS as a binding material can be beneficial for catalytic applications due to its large external surface area, flexible fibrous structure, and chemical resistance to both acid and basic media. A nano-zeolite-Y/CNS catalyst was successfully fabricated using a ball milling procedure, while creating a highly homogeneous structure with a high surface area of 874 m<sup>2</sup>/g compared to the commonly used alumina-supported industrial catalysts. The fabricated composite catalyst was tested for n-hexadecane cracking reaction and was compared to the catalytic activity of nano-zeolite-Y particles. Nano-zeolite-Y/CNS showed higher conversion towards n-hexadecane (80%) compared to nano-zeolite particles alone (66%). This showed that using CNS as a binding material for nano-zeolite-Y could solve the main drawback of nanoparticle agglomeration while creating a composite with homogeneous distribution of nano-zeolite-Y particles within the CNS matrix. High mechanical stability, and high accessibility to the catalytic sites of nano-zeolite-Y was achieved. Moreover, using CNS as a binder created a porous composite with a retained crystalline structure of nano-zeolite-Y particles. The nano-zeolite-Y/CNS composite showed high conversion of n-hexadecane and production of highly valuable alkenes and hydrogen gas.



Most of the hydrocarbon products were between C<sub>1</sub> and C<sub>7</sub>, propylene being the major hydrocarbon product. The aromatic products were toluene, benzene, naphthalene, cymene, and xylene. Moreover, zeolite-Y nanoparticles were seen to remain attached to CNS after being subjected to harsh cracking conditions inside the reactor, hence proving the catalyst's mechanical stability.

**Supplementary Materials:** The following are available online at <http://www.mdpi.com/2073-4344/10/12/1385/s1>, Figure S1: EDS analysis of an industrial hydrocracking catalyst extrudate received from local refinery in Abu Dhabi, United Arab Emirates, Figure S2: TGA graph of CNS, Table S1: Paraffins Carbon number in of NHYZ/CNS and NHYZ catalysts, Table S2: Olefins Carbon number in of NHYZ/CNS and NHYZ catalysts, Table S3: Decomposition Temperature of CNS.

**Author Contributions:** Supervision, conceptualization, visualization, investigation, and project administration was carried out by R.H. Catalytic testing was performed at the premises of ADNOC refining research center (ARRC) under supervision of G.S. Composite catalyst was developed and characterized by joint efforts of Saepurahman and B.Z. Data analysis and original draft preparation were carried out by cooperative efforts of S.F.A. and B.Z. All authors have read and agreed to the published version of the manuscript.

**Funding:** This research was partially funded by Abu Dhabi National Oil Company Research Center (ARRC).

**Acknowledgments:** The authors would like to thank ARRC for providing facilities for the catalytic reaction.

**Conflicts of Interest:** The authors declare that they have no known competing interest that could have appeared to influence the work reported in this paper.

## References

- Holderich, W.; Hesse, M.; Nömann, F. Zeolites: Catalysts for organic syntheses. *Angew. Chem. Int. Ed.* **1988**, *27*, 226–246. [CrossRef]
- Schulz, H.F.; Weitkamp, J.H. Zeolite catalysts. Hydrocracking and hydroisomerization of n-dodecane. *Ind. Eng. Chem. Prod. Res. Dev.* **1972**, *11*, 46–53. [CrossRef]
- Anis, S.F.; Singaravel, G.; Hashaikeh, R. Electropositive Ni-W/zeolite composite fibers for n-heptane hydrocracking and hydroisomerization. *Mater. Chem. Phys.* **2017**, *200*, 146–154. [CrossRef]
- Fechete, I.; Wang, Y.; Védrine, J.C. The past, present and future of heterogeneous catalysis. *Catal. Today* **2012**, *189*, 2–27. [CrossRef]
- Zecevic, J.; Vanbutsele, G.; De Jong, K.P.; Martens, J.A. Nanoscale intimacy in bifunctional catalysts for selective conversion of hydrocarbons. *Nature* **2015**, *528*, 245–248. [CrossRef] [PubMed]
- Jasra, R.V.; Tyagi, B.; Badheka, Y.M.; Choudary, V.N.; Bhat, T.S. Effect of clay binder on sorption and catalytic properties of zeolite pellets. *Ind. Eng. Chem. Res.* **2003**, *42*, 3263–3272. [CrossRef]
- Wu, X.; Alkhalil, A.; Anthony, R.G. Investigation on acidity of zeolites bound with silica and alumina. In *Studies in Surface Science and Catalysis*; Elsevier: Amsterdam, The Netherlands, 2000; pp. 217–225.
- Timken, H.K. Method for Preparing Titania-Bound Zeolite Catalysts. U.S. Patent 5,500,109, 4 July 1995.
- Chen, D.; He, L.; Shang, S. Study on aluminum phosphate binder and related Al<sub>2</sub>O<sub>3</sub>-SiC ceramic coating. *Mater. Sci. Eng. A* **2003**, *348*, 29–35. [CrossRef]
- Perego, C.; Bassi, G.; Girotti, G. Extruded Catalyst Based on Silica/Alumina Gel. U.S. Patent 20020099250A1, 4 November 2003.
- Bingre, R.; Louis, B.; Nguyen, P. An overview on zeolite shaping technology and solutions to overcome diffusion limitations. *Catalysts* **2018**, *8*, 163. [CrossRef]
- Wijngaarden, R.I.; Westerterp, K.R.; Kronberg, A.; Bos, A.N.R. *Industrial Catalysis: Optimizing Catalysts and Processes*; John Wiley & Sons: Hoboken, NJ, USA, 2008.
- Sun, H.; Shen, B.; Liu, J. N-Paraffins adsorption with 5A zeolites: The effect of binder on adsorption equilibria. *Sep. Purif. Technol.* **2008**, *64*, 135–139. [CrossRef]
- Chu, P.; Garwood, W.E. Catalytic Composition from Reaction of High Silica Zeolites with Binder. U.S. Patent 3308069A, 7 January 1986.
- Kauffman, J.W.; Hooks, P.A.; Nair, B.K.R. Method of Preparing an Alumina Catalyst Support and Catalyst for Dehydrogenation Reactions, and Its Use. U.S. Patent 9364815B2, 14 June 2016.
- Bartholomew, C.H. Mechanisms of catalyst deactivation. *Appl. Catal. A Gen.* **2001**, *212*, 17–60. [CrossRef]
- Anis, S.F.; Singaravel, G.; Hashaikeh, R. Hierarchical nano zeolite-Y hydrocracking composite fibers with highly efficient hydrocracking capability. *RSC Adv.* **2018**, *8*, 16703–16715. [CrossRef]

18. Anis, S.F.; Hashaikeh, R. Electrochemical water splitting using nano-zeolite Y supported tungsten oxide electrocatalysts. *J. Nanopart. Res.* **2018**, *20*, 47. [\[CrossRef\]](#)
19. Tosheva, L.; Valtchev, V.P. Nanozeolites: Synthesis, crystallization mechanism, and applications. *Chem. Mater.* **2005**, *17*, 2494–2513. [\[CrossRef\]](#)
20. Van Steen, E.; Prinsloo, F.F. Comparison of preparation methods for carbon nanotubes supported iron Fischer–Tropsch catalysts. *Catal. Today* **2002**, *71*, 327–334. [\[CrossRef\]](#)
21. Jiménez, V.; Sánchez, P.; Panagiotopoulou, P.; Valverde, J.L.; Romero, A. Methanation of CO, CO<sub>2</sub> and selective methanation of CO, in mixtures of CO and CO<sub>2</sub>, over ruthenium carbon nanofibers catalysts. *Appl. Catal. A Gen.* **2010**, *390*, 35–44. [\[CrossRef\]](#)
22. Coq, B.; Planeix, J.M.; Brotons, V. Fullerene-based materials as new support media in heterogeneous catalysis by metals. *Appl. Catal. A Gen.* **1998**, *173*, 175–183. [\[CrossRef\]](#)
23. Zheng, M.; Pang, J.; Wang, A.; Zhang, T. One-pot catalytic conversion of cellulose to ethylene glycol and other chemicals: From fundamental discovery to potential commercialization. *Chin. J. Catal.* **2014**, *35*, 602–613. [\[CrossRef\]](#)
24. Rodríguez-Reinoso, F. The role of carbon materials in heterogeneous catalysis. *Carbon* **1998**, *36*, 159–175. [\[CrossRef\]](#)
25. Bradley, J.P.; Brownlee, D.E.; Fraundorf, P. Carbon compounds in interplanetary dust: Evidence for formation by heterogeneous catalysis. *Science* **1984**, *223*, 56–58. [\[CrossRef\]](#)
26. Schrock, R.R. Multiple metal–carbon bonds for catalytic metathesis reactions (Nobel lecture). *Angew. Chem. Int. Ed.* **2006**, *45*, 3748–3759. [\[CrossRef\]](#) [\[PubMed\]](#)
27. Yang, Y.; Chiang, K.; Burke, N. Porous carbon-supported catalysts for energy and environmental applications: A short review. *Catal. Today* **2011**, *178*, 197–205. [\[CrossRef\]](#)
28. Zhang, J.; Liu, X.; Blume, R.; Zhang, A.; Schlögl, R.; Su, D.S. Surface-modified carbon nanotubes catalyze oxidative dehydrogenation of n-butane. *Science* **2008**, *322*, 73–77. [\[CrossRef\]](#) [\[PubMed\]](#)
29. Zhang, Q.; Kang, J.; Wang, Y. Development of novel catalysts for Fischer–Tropsch synthesis: Tuning the product selectivity. *ChemCatChem* **2010**, *2*, 1030–1058. [\[CrossRef\]](#)
30. Kong, H.; Zhou, M.; Lin, G.-D.; Hong-Bin, Z. Pt. catalyst supported on multi-walled carbon nanotubes for hydrogenation-dearomatization of toluene and tetralin. *Catal. Lett.* **2010**, *135*, 83–90. [\[CrossRef\]](#)
31. Shah, T.K.; Malecki, H.C.; Basantkumar, R.R.; Liu, H.; Fleischer, C.A.; Sedlak, J.J.; Patel, J.M.; Burgess, W.P.; Goldfinger, J.M. Carbon Nanostructures and Methods of Making the Same. U.S. Patent EP2900595A1, 26 September 2013.
32. Mahmoud, L.; Lalia, B.S.; Hashaikeh, R. Carbon nanostructures modified LiFePO<sub>4</sub> cathodes for lithium ion battery applications: Optimized porosity and composition. *Mater. Res. Express* **2016**, *3*, 125008. [\[CrossRef\]](#)
33. Khalil, A.; Lalia, B.S.; Hashaikeh, R. Nickel oxide nanocrystals as a lithium-ion battery anode: Structure-performance relationship. *J. Mater. Sci.* **2016**, *51*, 6624–6638. [\[CrossRef\]](#)
34. Zhuman, B.; Saepurahman; Anis, S.F.; Hashaikeh, R. Obtaining high crystalline ball milled HY zeolite particles with carbon nanostructures as a damping material. *Microporous Mesoporous Mater.* **2019**, *273*, 19–25. [\[CrossRef\]](#)
35. Anis, S.F.; Lalia, B.S.; Hashaikeh, R.; Hilal, N. Breaking through the selectivity-permeability tradeoff using nano zeolite-Y for micellar enhanced ultrafiltration dye rejection application. *Sep. Purif. Technol.* **2020**, *242*, 116824. [\[CrossRef\]](#)
36. Anis, S.F.; Hashaikeh, R.; Hilal, N. Flux and salt rejection enhancement of polyvinyl (alcohol) reverse osmosis membranes using nano-zeolite. *Desalination* **2019**, *470*, 114104. [\[CrossRef\]](#)
37. Anis, S.F.; Hashaikeh, R. Electrospun zeolite-Y fibers: Fabrication and morphology analysis. *Microporous Mesoporous Mater.* **2016**, *233*, 78–86. [\[CrossRef\]](#)
38. Brait, A.; Koopmans, A.; Weinstabl, H.; Ecker, A.; Seshan, K.; Lercher, J.A. Hexadecane conversion in the evaluation of commercial fluid catalytic cracking catalysts. *Ind. Eng. Chem. Res.* **1998**, *37*, 873–881. [\[CrossRef\]](#)
39. Abbot, J.; Wojciechowski, B. Kinetics of catalytic cracking of n-paraffins on HY zeolite. *J. Catal.* **1987**, *104*, 80–85. [\[CrossRef\]](#)
40. Plank, C.J. *The Invention of Zeolite Cracking Catalysts—A Personal Viewpoint*; ACS Publications: Washington, DC, USA, 1983.

41. Srinivas, B.; Maity, S.; Prasad, V.; Rana, M.S.; Kumar, M.; Dhar, G.M.; Rao, T. Support effect studies on TiO<sub>2</sub>-Al<sub>2</sub>O<sub>3</sub> mixed oxide hydroprocessing catalysts. In *Studies in Surface Science and Catalysis*; Elsevier: Amsterdam, The Netherlands, 1998; pp. 497–506.
42. Ulfah, M.; Octavia, S.; Suherman, H.; Laniwati, M.; Makerthiharta, I.G.B.N. Synthesis and characterization of modified  $\gamma$ -Alumina-NaA and  $\gamma$ -Alumina-NaX zeolite composites as methanol dehydration catalysts in synthesis Dimethyl Ether (DME). In *IOP Conference Series: Materials Science and Engineering*; IOP Publishing: Kupang, Indonesia, 2020.
43. Karami, D.; Mahinpey, N. Application of Novel Zeolite Y Nanoparticles in Catalytic Cracking Reactions. *Chem. Eng. Commun.* **2016**, *203*, 251–257. [[CrossRef](#)]
44. Vuong, G.-T.; Hoang, V.-T.; Nguyen, D.-T.; Do, T.-O. Synthesis of nanozeolites and nanozeolite-based FCC catalysts, and their catalytic activity in gas oil cracking reaction. *Appl. Catal. A Gen.* **2010**, *382*, 231–239. [[CrossRef](#)]
45. Bai, P.; Xie, M.; Etim, U.J.; Xing, W.; Wu, P.; Zhang, Y.; Liu, B.; Wang, Y.; Qiao, K.; Yan, Z. Zeolite Y mother liquor modified  $\gamma$ -Al<sub>2</sub>O<sub>3</sub> with enhanced Brönsted acidity as active matrix to improve the performance of fluid catalytic cracking catalyst. *Ind. Eng. Chem. Res.* **2018**, *57*, 1389–1398. [[CrossRef](#)]
46. Yin, H.; Zhou, T.; Liu, Y.; Chai, Y.; Liu, H. NiMo/Al<sub>2</sub>O<sub>3</sub> catalyst containing nano-sized zeolite Y for deep hydrodesulfurization and hydrodenitrogenation of diesel. *J. Nat. Gas Chem.* **2011**, *20*, 441–448. [[CrossRef](#)]
47. Hashaikh, R. Insight into ball milling for size reduction and nanoparticles production of HY zeolite. *Mater. Chem. Phys.* **2018**, *220*, 322–330.
48. John, T.M.; Wojciechowski, B.W. On identifying the primary and secondary products of the catalytic cracking of neutral distillates. *J. Catal.* **1975**, *37*, 240–250. [[CrossRef](#)]
49. Swisher, J.A.; Hansen, N.; Maesen, T.; Keil, F.J.; Smit, B.; Bell, A.T. Theoretical simulation of n-alkane cracking on zeolites. *J. Phys. Chem. C* **2010**, *114*, 10229–10239. [[CrossRef](#)]
50. Corma, A.; Planelles, J.; Sánchez-Marín, J.; Tomás, F. The role of different types of acid site in the cracking of alkanes on zeolite catalysts. *J. Catal.* **1985**, *93*, 30–37. [[CrossRef](#)]
51. Guisnet, M.; Gilson, J.-P. *Zeolites for Cleaner Technologies*; World Scientific: Singapore, 2002; Volume 3.
52. Planelles, J.; Sanchez-Marin, J.; Tomas, F.; Corma, A. On the formation of methane and hydrogen during cracking of alkanes. *J. Mol. Catal.* **1985**, *32*, 365–375. [[CrossRef](#)]
53. Commeyras, A.; Olah, G.A. Chemistry in super acids. II. Nuclear magnetic resonance and laser Raman spectroscopic study of the antimony pentafluoride-fluorosulfuric acid (sulfur dioxide) solvent system (magic acid). The effect of added halides, water, alcohols, and carboxylic acids. Study of the hydronium ion. *J. Am. Chem. Soc.* **1969**, *91*, 2929–2942.
54. Olah, G.A.; DeMember, J.R.; Shen, J. Electrophilic reactions at single bonds. X. Hydrogen transfer, alkylation, and alkylolysis of alkanes with methyl and ethyl fluoroantimonate. *J. Am. Chem. Soc.* **1973**, *95*, 4952–4956. [[CrossRef](#)]
55. Abbot, J.; Wojciechowski, B. The mechanism of paraffin reactions on HY zeolite. *J. Catal.* **1989**, *115*, 1–15. [[CrossRef](#)]

**Publisher's Note:** MDPI stays neutral with regard to jurisdictional claims in published maps and institutional affiliations.



© 2020 by the authors. Licensee MDPI, Basel, Switzerland. This article is an open access article distributed under the terms and conditions of the Creative Commons Attribution (CC BY) license (<http://creativecommons.org/licenses/by/4.0/>).